

Synthesis of magnetic N-doped carbon dots as pH-responsive targeted molecule cargo and its antioxidant and antibacterial behaviour

HAYAT ALZHRANI

MOHAMMED S. ALKALTHAM

TAWFIQ ALSULAMI

ABDULHAKEEM ALZHRANI

SULEIMAN A ALTHAWAB*

Department of Food Science & Nutrition, College of Food and Agricultural Sciences, King Saud University, Riyadh 11451, Saudi Arabia

* Correspondence; e-mail: salthawab@ksu.edu.sa

ABSTRACT

This study successfully generated magnetic N-doped carbon dots (CDs-MNPs) that exhibit two distinct functions: pH-responsive targeted drug delivery and powerful antioxidant action. The structural integrity, magnetic characteristics, and thermal stability of the samples were confirmed using comprehensive characterization techniques such as scanning electron microscopy, superconducting quantum interference device, Fourier Transform Infrared Spectroscopy, X-ray diffraction, continuous-wave electron paramagnetic resonance, X-ray photoelectron spectroscopy, surface porosity and Thermogravimetric analysis. The CDs-MNPs displayed pH-dependent drug release profiles that conformed to zero-order, Higuchi, and Peppas models, demonstrating their ability to provide regulated release. The antioxidant activity of the carbon dots was assessed using the DPPH assay, where the radical scavenging capacity exceeded 80%. This high level of activity was attributed to the synergistic effects of nitrogen doping and the functional groups present on the carbon dots. The biocompatibility of the specimen (upto 100 mg/mL), which is essential for

biomedical applications, was confirmed by MTT assays. This study highlights the potential of CDs-MNPs as an effective option for therapeutic interventions, providing customized drug delivery and antioxidant advantages. The antibacterial activity of CDs-MNPs was evaluated against gram-negative *Escherichia coli* and gram-positive *Staphylococcus aureus* bacterial strains, demonstrating significant efficacy. These results highlight the potential of CD-based nanobactericides for applications in biomedical and food monitoring.

Keywords: carbon dots, magnetic nanocomposite, antioxidant, drug release

Accepted May 28, 2025

Published online June 1, 2025

INTRODUCTION

The chemical stability, high water dispersibility, and remarkable biocompatibility of carbon dots (CDs), a class of fluorescent carbon nanoparticles smaller than 20 nm, have led to their extensive use in various biomedical applications (1, 2). CDs were accidentally discovered while purifying single-walled carbon nanotubes, but now they can be easily synthesized from a wide variety of materials using methods such as electrochemical exfoliation, liquid phase exfoliation, hydrothermal/solvothermal treatment, stepwise organic synthesis from smaller precursors, and microwave-mediated synthesis (3-6). There are three distinct types of CDs: graphene quantum dots (GQDs), polymer dots, and carbon quantum dots (CQDs). Nanostructure, creation mechanism, and distinctive features are the primary criteria for their categorization (7). Chemical groups can be found on the surface or within the graphite layers of GQDs, which might contain one or more layers. The lateral dimensions of GQDs are larger than their vertical dimensions, making them anisotropic (8). Oxide cutting of larger graphitized materials is the standard method for obtaining CDs of this type (9). In contrast, CQDs and carbonized polymer dots are commonly made from small molecules, polymers, or biomass and typically have spherical shapes. They are generated by assembling, crosslinking, polymerizing, and carbonizing graphite structures with multiple layers, whereas carbonized polymer dots contain core-shell structures that are unique to them (10). Typically, carbonized polymer dots have carbon cores that are smaller than 20 nm and are encased in shells made of different functional groups or polymer chains (11); this gives these

dots excellent stability and minimal toxicity (12, 13). CDs have been effectively utilized in several fields such as bioimaging (14), catalysis (15), sensors (16), and drug delivery (17, 18). Significant advancements have been made in drug loading (19). It is widely recognized that delivering medications without targeting can lead to toxicity in healthy cells (20). However, employment of CD delivery methods can alleviate this issue. For example, research has demonstrated that CDs can serve as nanocarriers for doxorubicin (DOX), an anticancer medicine. The CD loading method has been found to have superior anti-tumour effects compared to free DOX, effectively suppressing tumour growth and enhancing targeted therapy. The Jia group utilized polyethylene glycol (PEG) modified CDs to enhance the delivery of specific medications to the tumour microenvironment. This approach effectively minimized drug leakage in the physiological medium and mitigated the drug's negative effects, thereby significantly enhancing the anti-tumour efficacy of DOX (21).

Various types of nanoparticles, such as liposomes (22), niosomes (23), lipid-based nanoparticles (24), and polymeric nanoparticles (25), have been investigated regarding their role in enhancing the therapeutic effectiveness of drugs. However, it is important to note that the utilisation of these nanoparticles is subject to certain constraints. Magnetic carbon dots (CDs-MNPs) are now recognized as crucial components in the field of nanotechnology because of their distinctive blend of magnetic and luminous characteristics (26). These magnetic nanoparticles (MNPs) display exceptional qualities, such as high stability, minimal harm to living organisms, and adjustable optical properties, which make them highly favourable options for various uses (27-29). CDs-MNPs have the capacity to significantly transform a wide range of sectors, including biomedical imaging, medication delivery, environmental remediation, and catalysis (30). This paper explores the process of creating, describing, and utilizing CDs-MNPs, providing insight into their crucial role in furthering scientific and technological progress. In addition, CDs-MNPs have numerous benefits compared to conventional nanoparticles such as metallic nanoparticles (e.g., gold, silver) (31, 32) and inorganic nanoparticles (e.g., silica, titanium dioxide) (33), in the context of drug delivery applications (34). Their magnetic qualities allow for easy manipulation and targeting when exposed to external magnetic fields, which facilitates accurate delivery to specified tissues or cells. Additionally, the adjustable surface chemistry of CDs-MNPs enables effective loading and precise release of therapeutic molecules, improving the efficiency of drug delivery while reducing unintended side effects (35, 36). CDs-MNPs are highly desirable for biomedical

applications due to their excellent biocompatibility and minimal cytotoxicity (37). They thus provide a safer and more efficient alternative to traditional drug delivery systems.

The present study involved the development and analysis of a sophisticated nanoprobe utilizing CDs-MNPs. This system was modified with folic acid to improve the effectiveness of a model cancer drug that is both non-toxic and hydrophobic (38). Subsequently, a CDs-MNPs nanocomposite was prepared using a single-step coprecipitation technique. The nanoparticles were magnetically separated, and the nanocomposite was conjugated with folic acid using EDC/NHS coupling chemistry. To examine the pH sensitivity of the synthesized nanoparticles, we evaluated how the model drug molecule is released in different pH systems. A cytotoxicity study was also employed to evaluate the nanocarrier's suppressive impact on fibroblast cells. The findings of our study demonstrate that the CDs-MNPs-anchored folic acid nanoparticles have significant potential as a pH-responsive and cost-effective method for delivering hydrophobic anticancer medicines to specific targets.

Experimental

Materials

Chitosan (medium molecular weight) was purchased from Sigma (Germany). 1-Ethyl-3-(3-dimethylamino propyl)-carbodiimide (EDC), Folic acid (FA), curcumin, Ferrous-sulphate-heptahydrate ($\text{FeSO}_4 \cdot 7\text{H}_2\text{O}$), Iron(III) sulfate hydrate ($\text{Fe}_2(\text{SO}_4)_3 \cdot x\text{H}_2\text{O}$), N-hydroxysulfoxuccinimide (sulfo-NHS), and 3-(4,5-Dimethylthiazol-2-yl)-2,5-diphenyltetrazolium bromide (MTT) were acquired from (Merck, Germany) and used as received. Lemon was procured from the local market. Other solvents and inorganic salts were used without further purification.

Characterizations

The morphology of the prepared CDs was analyzed using an FEI Tecnai G2 F20 transmission electron microscope (TEM, Hitachi, Japan). ImageJ software was used for the TEM size-distribution analysis of the CDs. We utilized a Vetex 70 Fourier Transform Infrared (FT-IR) spectrometer from Bruker Corp. (Germany) to conduct FT-IR spectrum analysis and gain insights into the structure of CDs. To examine the composition of CDs, we conducted X-ray photoelectron

spectroscopy (XPS) measurements using the Thermo Scientific K-Alpha spectrometer from Thermo Fisher Scientific (Waltham, MA, USA). The UV–vis absorption spectra were collected using a UV-2600 spectra photometer (Shimadzu, Japan) with a 1.0 cm optical path length. All the fluorescence spectra measurements in this study were obtained using a Horiba FluoroMax-4 spectrometer (Horiba, USA).

Synthesis of CDs

The N-doped CDs were synthesized by thermally coupling a combination of chitosan and lemon juice (extract). A solution containing 28 mg of chitosan and 10 mL of lemon juice was prepared by dissolving the two in 40 mL of water. Next, the whole solution was transferred to a Teflon-lined steel autoclave. The autoclave was placed into 180 °C oven and kept for 8 h. After completion, the whole system was cooled to room temperature, followed by purification through a 0.22 microfiltration unit. The colloidal system of chitosan-lemon-juice-derived CDs was subjected to dialysis against Milli-Q water using a semi-permeable membrane (specifically, a cellulose ester membrane bag with an average molecular weight of 3500 Da). The CDs were then lyophilized in a vacuum, resulting in the production of a dark brown powder with a yield of approximately 32.8%.

Synthesis of Magnetic Carbon Dots

The synthesis of carbon dots-magnetic nanoparticles-based nanocomposite (CDs-MNPs) was achieved using a modified co-precipitation process. Firstly, the CDs that were synthesized were evenly distributed in distilled water to obtain a concentration of 0.6 mg/mL. The dispersion was sonicated for 25 minutes to ensure uniformity. Under a nitrogen environment, 0.65 g of iron (+3) chloride hexahydrate ($\text{FeCl}_3 \cdot 6\text{H}_2\text{O}$) was added to a 100 mL homogeneous dispersion. The addition was done at room temperature with constant stirring. Afterwards, the mixture was heated to a temperature of 80 °C. Then, 0.35 g of iron (+2) sulphate heptahydrate ($\text{FeSO}_4 \cdot 7\text{H}_2\text{O}$) was added and agitated for an additional 30 minutes. After the reaction was finished, the pH of the solution was raised to ~10 by gradually adding ammonia. The resultant black precipitate, comprising CDs-MNPs, was separated using a magnet and meticulously rinsed with deionized water multiple times to eliminate any unreacted contaminants. The refined product was subsequently stored at a temperature of 4 °C for further characterisation and analysis.

Synthesis of Folic-Acid-Functionalized CDs-MNPs (F-CDs-MNPs)

Folic acid was conjugated to the hybrid of CDs-MNPs by utilizing EDC and NHS as activating agents. During this procedure, the carboxylic acid groups on the CDs-MNPs were stimulated by EDC to generate reactive intermediates that can establish amide bonds with the amine groups of folic acid. To activate the carboxyl groups, a mixture of 5 mL of the CDs-MNPs dispersion (1.2 mg/mL), 85 mg of EDC, and 62 mg of NHS was agitated for 2 hours. Afterwards, 9.4 mg of folic acid was introduced into the active mixture. The reaction was then carried out for 20 hours at room temperature with continuous stirring in a dark atmosphere to prevent photodegradation. After the reaction, the surplus folic acid and unreacted EDC and NHS were eliminated by rinsing the product multiple times with deionized water and using a magnet to separate the conjugated CDs-MNPs, which are named F-CDs-MNPs. Subsequently, the end product underwent freeze-drying and was subsequently stored at a temperature of 4 °C for subsequent characterization and analysis.

Antioxidant Activity

The detailed methodology for the antioxidant study is provided in the supplementary materials.

Drug Loading and Release Kinetics Study

The process of loading drugs (here curcumin) onto CDs-MNPs involved incubating various doses of curcumin (0.5, 1, 2, and 4 mg/mL; solubilized in 50% ethanol-water mixture) with a dispersion of CDs-MNPs (0.5 mg/mL) for 24 hours at room temperature in a light-protected environment to avoid deterioration caused by light. Following the incubation period, a magnet was employed to isolate the curcumin-loaded CDs-MNPs from the system. The isolated product was subsequently washed thrice with a solution of deionized water and ethanol until the liquid above it was transparent and without any colour, indicating the elimination of any curcumin that was not bonded. The concentration of curcumin that was loaded onto the nanoparticles was determined indirectly by measuring the absorbance of the liquid remaining after the nanoparticles were separated at a wavelength of 430 nm. Similar techniques were employed to use this procedure to load curcumin onto the F-CDs-MNPs, ensuring successful loading of curcumin onto the modified nanoparticles. The loading efficiency (LE) was calculated by determining the mass of the drug that was successfully incorporated into the nanoparticles and comparing it to the total mass of the drug-

loaded nanoparticles. This value was then expressed as a percentage to reflect the efficiency of the loading process.

The method used to evaluate the release of curcumin from the CDs-MNPs nanocarrier involved dispersing the curcumin-loaded CDs-MNPs (0.5 mg of drug per 1 mg of CDs-MNPs) in a dialysis bag with a molecular weight limit of 3.5 kDa. The bag was thereafter subjected to dialysis against a 50-mL solution of phosphate-buffered saline (PBS) with a concentration of 120 mM and a pH of 5.6. The dialysis process was carried out at a temperature of 37 °C, with continuous shaking at a speed of 100 rpm. To address the issue of curcumin's low solubility in PBS, a solution of Tween-80 at a concentration of 0.5% w/v was added to the buffer. This addition helped to enhance the release of curcumin. The same methodology was utilised to assess the release characteristics of curcumin from the F-CDs-MNPs. The cumulative release percentage was calculated by measuring the amount of curcumin released at specific time intervals and comparing it to the total amount of curcumin initially loaded onto the nanoparticles. This allowed for the evaluation of the release profile over time as a percentage of the original drug content.

Cytotoxicity Assay

An MTT experiment was used to evaluate the cytotoxic effects of magnetic nanoparticles on the 3T3 fibroblast cell line. The cells were placed in 96-well plates with a density of 1.48×10^4 cells per well and incubated at 37°C in a 5% CO₂ environment for 24 hours to promote cell adhesion. Afterwards, the cells were subjected to different doses of the nanoparticles by replacing the medium in each well with 100 µL of complete DMEM containing the nanoparticles. Control wells were kept with cells only (negative control) and with a known harmful chemical (positive control). The plates were further incubated for an additional 24 hours under identical circumstances. Following the incubation period, the medium was extracted, and 100 µL of MTT solution (5 mg/mL in PBS, subjected to filtration sterilisation) was introduced into each well. The plates were subsequently placed in an incubator at a temperature of 37°C and a carbon dioxide concentration of 5% for a duration of 4 hours. Subsequently, the MTT solution was meticulously removed from each well, and 100 µL of DMSO was introduced to dissolve the formazan crystals. The plates were agitated for 10 minutes at ambient temperature to ensure the crystals were fully dissolved. The absorbance at a wavelength of 570 nm was determined using a microplate reader. Wells containing only DMSO were used as blank controls to compensate for background absorbance. Cell viability

is calculated as the percentage of absorbance in the sample. Every condition was evaluated three times to guarantee statistical significance, and sterile conditions were consistently upheld during the procedure to prevent contamination.

Antibacterial Activity Evaluation

Details of the antibacterial study using CDs-MNPs against both gram-positive and gram-negative bacteria is provided in the supplementary materials

Statistical Analysis

All tests were performed in triplicate, and the experimental results were presented as mean \pm standard deviation (SD). A one-way analysis of variance (ANOVA) was performed, and differences ($p < 0.05$) between individual means were analyzed via Duncan's multiple range test utilizing the SPSS statistical analysis computer program (SPSS Inc., Chicago, IL, USA).

Results and discussion

Synthesis and Morphology

The synthesis of CD-based magnetic nanocomposite was prepared via a sequential synthesis process where the initial step was the CD synthesis using a one-step hydrothermal process and the second step was the coprecipitation process. The process of synthesizing nanomaterials is visually represented in Figure 1. The procedure commences by combining chitosan, a naturally occurring biopolymer, with lemon extract. Lemon juice serves as a natural carbon precursor and a source of citric acid, which undergoes hydrothermal carbonization to form CDs. The organic acids and polyphenols present in lemon juice contribute to the nucleation and growth of CDs, while also providing surface functional groups such as hydroxyl (-OH) and carboxyl (-COOH) that enhance the water dispersibility and stability of the resulting nanomaterial (39). Additionally, these functional groups facilitate interactions with magnetic nanoparticles (MNPs) and folic acid, aiding in the formation of the F-CDs-MNPs composite. This mixture is then exposed to hydrothermal treatment, resulting in the production of CDs. Hydrothermal synthesis is essential for transforming the chitosan-lemon combination into nanoscale CDs, which act as the foundational structure for subsequent modification. In the subsequent step, the CDs are co-precipitated with iron ions (Fe^{3+}

and Fe^{2+}), resulting in the formation of CDs-MNPs. This process successfully integrates magnetic characteristics into the carbon dots, resulting in the formation of CDs-MNPs. The co-precipitation procedure guarantees the uniform dispersion of magnetic characteristics, which is a crucial aspect for the envisaged biomedical uses (40). After the formation of CDs-MNPs, the surface of these nanostructures was altered by attaching folic acid using EDC/NHS coupling chemistry. The last stage entailed the deposition of curcumin, a biologically active substance, onto the surface of the CDs-MNPs. The illustration in Figure 1 also includes a high-resolution scanning electron microscopy (HRSEM) image in the lower left corner, which offers a detailed view of the CDs-MNPs. The Figure S2 displays a densely packed and grainy structure with extremely small characteristics, providing evidence of the successful creation of the nanomaterial. The figure presents a comprehensive transmission electron microscopy (TEM) analysis of CDs, MNPs, and their nanocomposites. Figure S2 (a) displays a high-magnification TEM image of CDs, revealing their nanoscale morphology and dispersion. Figure S2 (b) provides a statistical size distribution analysis of the CDs, obtained using ImageJ software, showing a mean particle size in the range of 2–6 nm, with a Gaussian-like distribution curve indicating a relatively narrow size distribution. Figure S2 (c)–(e) illustrate the structural characteristics of different nanoparticle systems. Panel (c) depicts pure MNPs, showing a dense cluster of black contrast regions attributed to the high electron density of the magnetic particles. Figure S2 (d) represents CDs-MNPs nanocomposites, where CDs appear well-integrated with MNPs, suggesting successful hybridization. Finally, Figure S2 (e) exhibits drug-loaded CDs-MNPs nanocomposites, characterized by a more heterogeneous structure, possibly due to the encapsulation of drug molecules within the composite matrix.

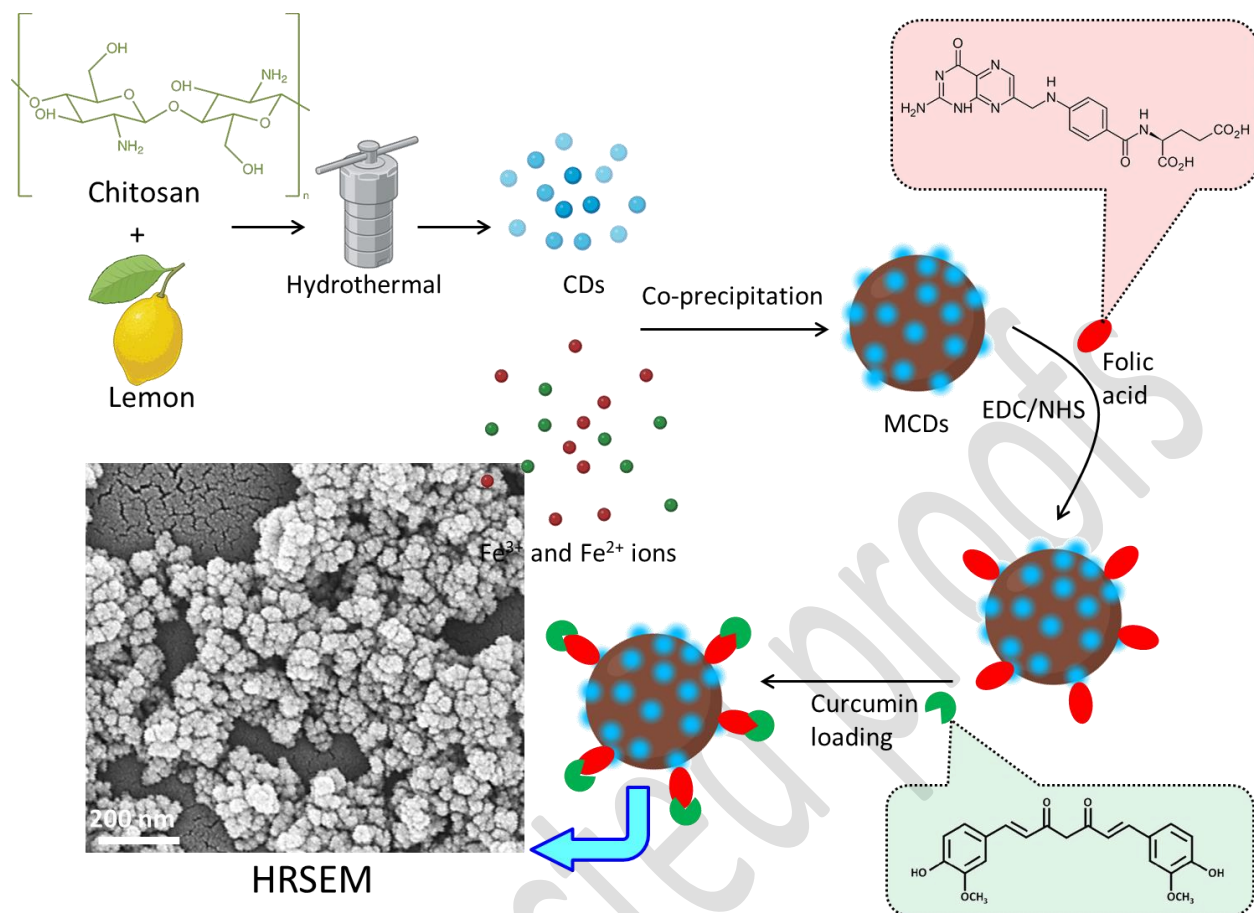


Figure 1: Schematic of CD-MNP nanocomposite preparation. CDs were synthesized via a hydrothermal method using chitosan and lemon, followed by co-precipitation with Fe³⁺/Fe²⁺ ions to form MCDs. Functionalization with folic acid via EDC/NHS chemistry and curcumin loading enhanced targeting and therapeutic potential. The HRSEM image shows the nanostructured morphology with ~200 nm particles.

Magnetic and Surface Properties

The magnetic characteristics of MNPs without any additional coating and the hybrid of CDs-MNPs were examined at room temperature using a SQUID, as illustrated in Figure 2a. Both nanoparticles demonstrate little remanence and coercivity, which suggests superparamagnetic behaviour (41). In addition, the saturation magnetization (M_s) values were measured to be 74.7 emu/g and 61.1 emu/g for MNPs and CDs-MNPs, respectively. The lower M_s value obtained for CDs-MNPs in comparison to bare MNPs can be attributed to the diamagnetic properties of CDs. Although there

has been a decrease in size, CDs-MNPs can still be easily separated using an external magnet because of their magnetic properties.

FTIR spectroscopy was used to analyse the surface functional groups of CDs, MNPs, CDs-MNPs, and F-CDs-MNPs. Per Figure 2b, the spectra of MNPs display a distinct peak at around 579 cm^{-1} , which signifies the existence of $-\text{Fe}-\text{O}$ bonds that are commonly found in magnetite production (42). The QDs exhibit two prominent peaks at 1382 cm^{-1} and 1639 cm^{-1} , which can be attributed to the stretching vibration of the $-\text{OH}$ group in the $-\text{COOH}$ group and the $\text{C}-\text{C}$ bonds, respectively. In addition, a peak detected at 1119 cm^{-1} corresponds to $\text{C}-\text{N}$ stretching functional groups, whereas wide bands ranging from 3000 to 3400 cm^{-1} indicate stretching vibrations of $-\text{OH}$ and $-\text{NH}$ groups. The FTIR spectrum of CDs-MNPs exhibits the distinctive peaks of both CDs and MNPs, providing confirmation of effective hybridization. In addition, the FTIR study also presents evidence of the bonding of folic acid to CDs-MNPs nanoparticles, as shown in Figure 2b. The spectrum of F-CDs-MNPs has prominent peaks at 1640 cm^{-1} and 1402 cm^{-1} , which correspond to the distinctive properties of folic acid. Specifically, the peak at 1639 cm^{-1} indicates the stretching of the aromatic ring in the pteridine ring, while the peak at 1402 cm^{-1} represents the p-amino benzoic acid moiety.

XRD studies were performed to the MNPs and CDs-MNPs nanoparticles, as seen in Figure 2c. The XRD analysis revealed the presence of six well-defined peaks at specific angles (2θ values) of 30.11° , 35.38° , 43.02° , 53.57° , 56.94° , and 62.72° ; these peaks correspond to the crystallographic planes (220), (311), (400), (422), (511), and (440), respectively. This confirms the successful synthesis of MNP nanoparticles (42). The consistent pattern that emerges for CDs-MNPs implies that the crystalline structure of magnetite remains unaltered during hybridization. The lack of discernible CD signals can be ascribed to the low concentration, high dispersion, and limited crystallinity of CDs inside the CDs-MNPs nanocomposite (43).

Figure 2d displays the CW-EPR spectra obtained in X-band (9.79 GHz) for the MNPs and CDs-MNPs nanocomposites. At normal temperature, a wide and powerful single asymmetry resonance signal is detected at a magnetic field strength of around $\sim 3200\text{ Oe}$. The broadening of the resonance line can be ascribed to spin disorder, which likely arises from mostly antiferromagnetic interaction between adjacent spins in magnetic nanoparticles (44). The broadening of these lines may be attributed to the dipolar interaction between superparamagnetic nanoparticles (45).

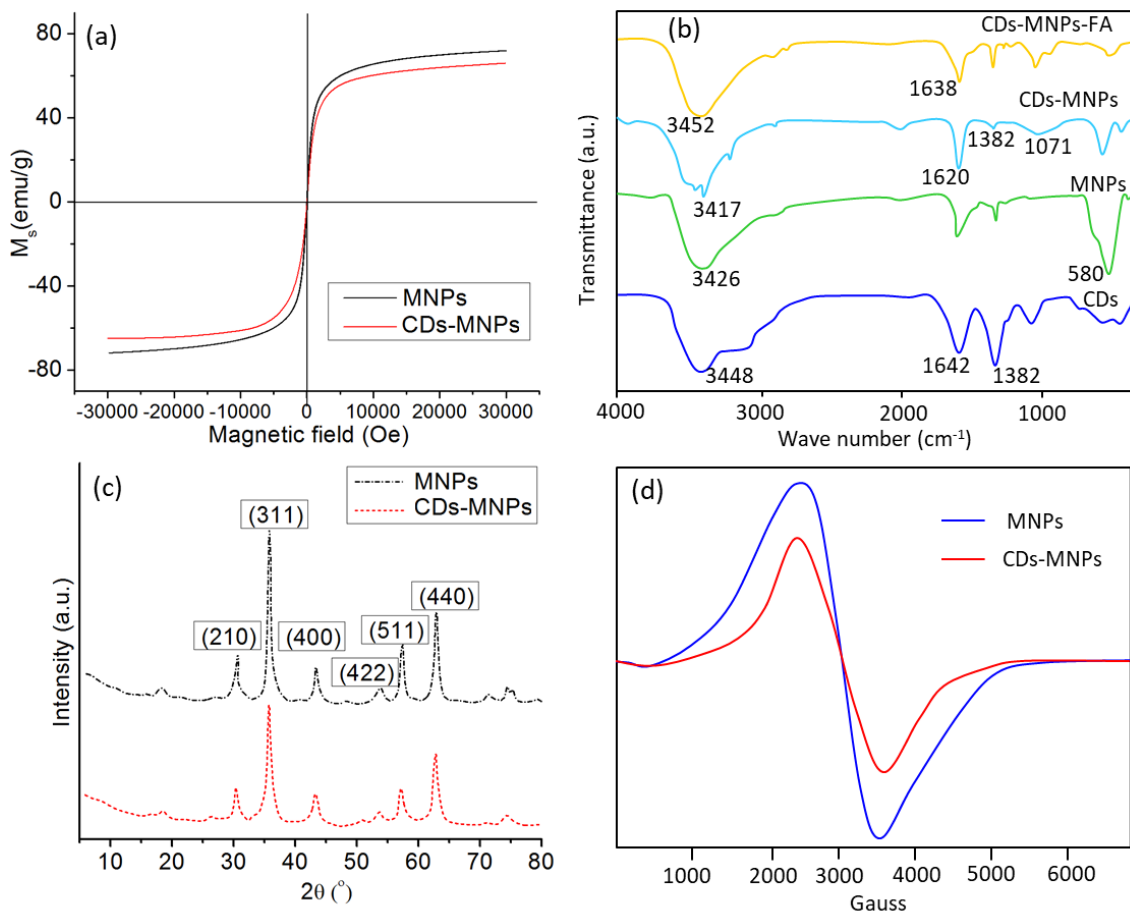


Figure 2: (a) SQUID analysis of the MNPs and CDs-MNPs nanocomposite. (b) FTIR spectra of pure CDs, MNPs, CDs-MNPs composite, and F-CDs-MNPs composite. (c) XRD of MNPs and CDs-MNPs. (d) EPR spectra of MNPs and CDs-MNPs.

The optical characteristics of CDs were examined through UV-visible and fluorescence spectroscopy, and the details are given in the supporting information. The X-ray photoelectron spectroscopy (XPS) data for the CDs-MNPs nanocomposite provides essential insights into the surface composition and bonding environments of the material. The survey spectrum (Figure 3a) revealed the presence of carbon, nitrogen, oxygen, and iron. The high-resolution XPS spectra of the C1s peak (Figure 3b) showed peaks at ~ 284.5 eV, 285.8 eV, and 288.4 eV, corresponding to the C=C/C-C, C-O/C-N bonds, and carbonyl C=O groups, respectively(46-48). The N1s spectrum (Figure 3c) showed peaks at ~ 400.2 eV and ~ 401.4 eV, ascribed to the C-N bonds and N-H, respectively. The spectrum of Fe2p (Figure 3d) exhibited two distinct peaks associated with Fe $2p_{3/2}$ (~ 711 eV) and Fe $2p_{1/2}$ (~ 724 eV)(47, 49).

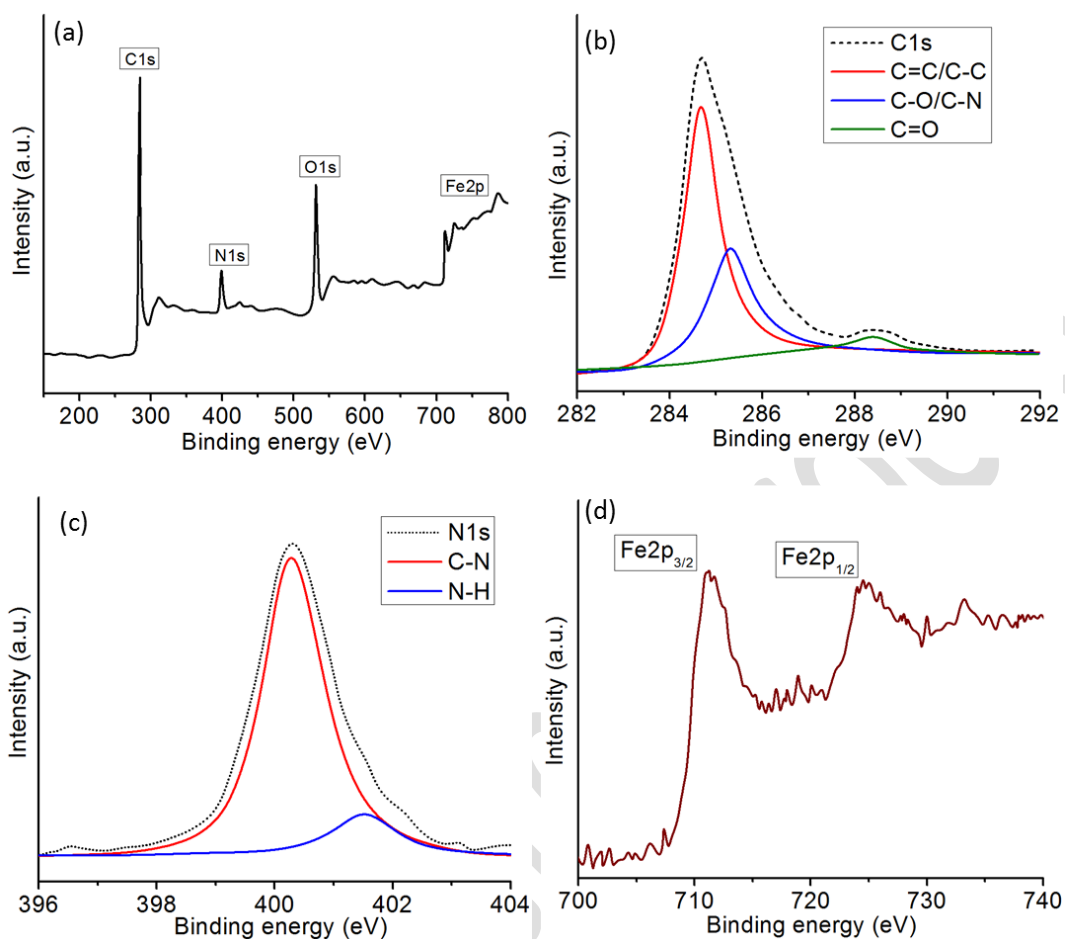


Figure 3: (a) XPS survey spectra of CDs-MNPs nanocomposite. High resolution XPS spectra of (b) C1s, (c) N1s, and (d) Fe2p.

Thermal Property and BET

Figure 5a illustrates the thermogravimetric analysis (TGA) curves of MNPs and CDs-MNPs nanocomposite. The TGA plot of pure MNPs typically exhibits a decrease in weight as temperature increases. At lower temperatures (about room temperature to 100 °C), there is usually a minimal decrease in weight; this is caused by the elimination of water molecules that are physically attached to the surface of Fe₃O₄. At temperatures above 200 °C, a substantial decrease in weight occurs, indicating the breakdown of Fe₃O₄ into Fe₂O₃ (50, 51). The breakdown process persists until around 600 °C, resulting in a progressive decrease in weight caused by the oxidation of Fe₃O₄ to Fe₂O₃. Beyond 600 °C, the decrease in weight stops because Fe₂O₃ remains unchanged even with more heating. CDs-MNPs exhibit two clearly identifiable stages of weight reduction. The initial

weight loss, which takes place at temperatures ranging from 110 °C to 150 °C, is caused by the removal of water that is adsorbed on the surface of the nanoparticles. The weight loss that follows, occurring within the temperature range of 180 °C to 330 °C, is attributed to the disintegration of CDs. The weight loss difference between these two systems could be attributed to the relative mass ratios present in their composition.

The BET isotherm study of MNPs and CDs-MNPs provides valuable information regarding their surface area and pore structure. The isotherm for MNPs, per Figure 5b, exhibits a substantial augmentation in the amount of gas adsorbed, reaching around 150 cm³/g (standard temperature and pressure) at a relative pressure (p/p_0) of roughly 0.98. This suggests a large amount of surface area that can be used for adsorption, which is a common feature of materials with vast porous structures. At relative pressures below 0.1 ($p/p_0 < 0.1$), the volume of adsorption presents a slow increase, indicating that the initial adsorption is limited due to the smaller surface area available for gas molecules. The isotherm displays a Type IV characteristic, characterized by a hysteresis loop that initiates at a relative pressure of approximately 0.45 and concludes at 0.95, supporting the presence of mesoporous materials. The hysteric loop indicates the occurrence of capillary condensation in the pores, which confirms the existence of mesopores in the structure of the MNPs. Similarly, the BET isotherm for CDs-MNPs (Figure 5c) demonstrates that the gas adsorption volume likewise reaches ~150 cm³/g (STP) at a relative pressure of ~0.98. The adsorption rate is higher at lower pressures when compared to MNPs, indicating a larger initial surface area resulting from the presence of CDs. The isotherm of CDs-MNPs exhibits Type IV behavior, characterized by a hysteresis loop that begins at roughly 0.4 and concludes at around 0.95. By including CDs in the composite, the mesoporous structure is preserved, and the pore system becomes more intricate, perhaps leading to improved adsorption capabilities for the material. The pore size distribution of both MNPs and CDs-MNPs, as shown in Figure 5d, reveals a dominant peak in the range of 10–20 nm. MNPs exhibit a distinct peak at around 15 nm, whereas CDs-MNPs exhibit a slightly wider peak in the same size range. The total pore volume of the magnetic nanoparticles (MNPs) reaches a maximum of about 0.018 cm³ per gram per nanometer, when the pore diameter is approximately 15 nm. The CDs-MNPs exhibit a peak cumulative pore volume of around 0.017 cm³/g·nm, indicating a comparable overall pore volume and distribution. However, the introduction of CDs effects in extent of physical crosslinking resulting higher pore formation. Overall, the BET isotherm analysis reveals that both MNPs and CDs-MNPs exhibit substantial surface areas and

mesoporous properties. The adsorption capacities, characterized by gas volumes adsorbing ~ 150 cm^3/g , demonstrate their appropriateness for applications that necessitate materials with extensive surface areas and clearly defined pore structures. Combining CDs with MNPs creates a composite material that has the potential for increased surface area and more intricate pore structure. This makes the material beneficial for a range of applications where having a large surface area and porosity is crucial, including catalysis, adsorption, and drug delivery.

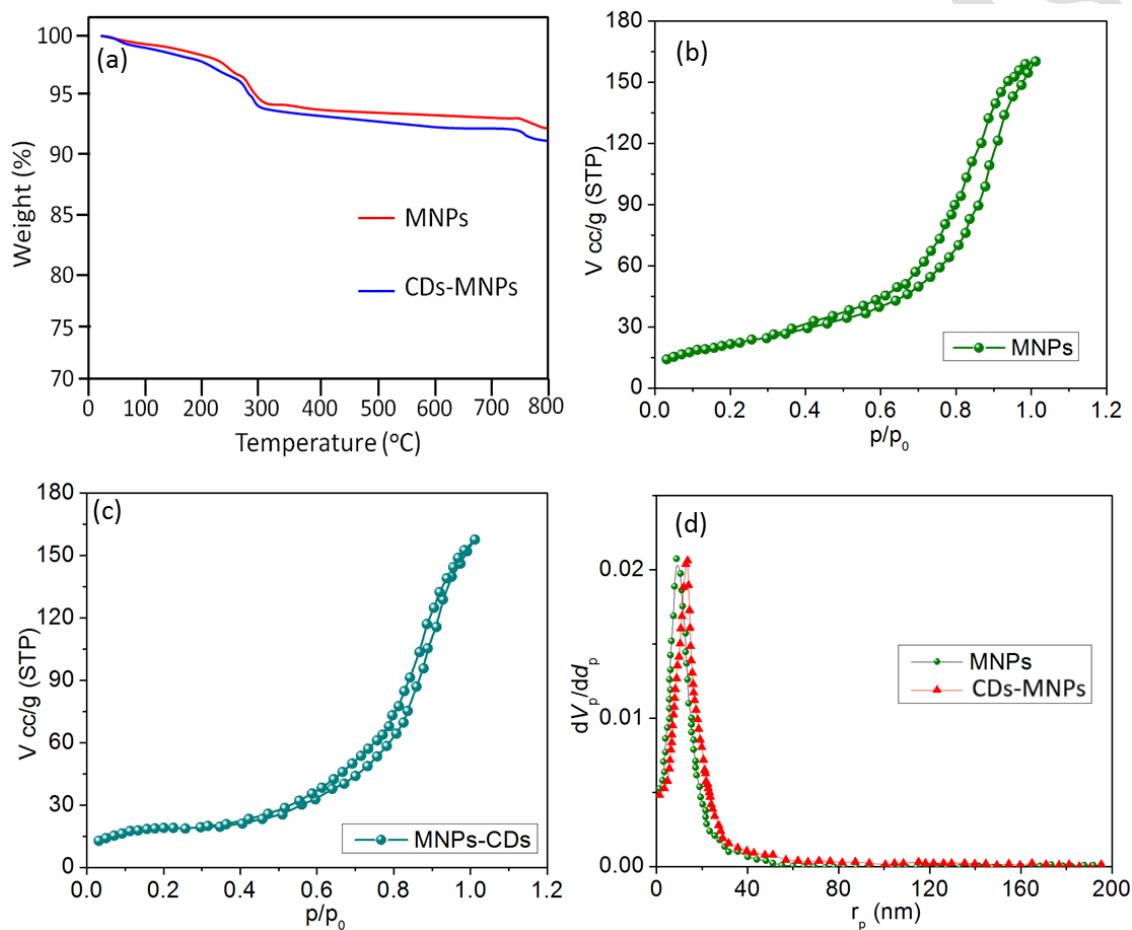


Figure 4: (a) TGA plot of MNPs and CDs-MNPs nanocomposite. (b) N₂ adsorption–desorption (BET) isotherms of Fe₃O₄ (MNPs). (c) N₂ adsorption–desorption (BET) isotherms of CDs-MNPs. (d) pore size distribution of MNPs and CDs-MNPs nanocomposites.

Antioxidant Activity

The antioxidant activity of CDs-MNPs nanocomposites was assessed *in vitro* at 517 nm using the DPPH free radical spectroscopy technique (see Figure 5). The DPPH test relies on electron

transport principles to generate a stable free radical at ambient temperature. The presence of an antioxidant compound reduces this free radical, resulting in a colour change from violet to colourless. Figures 7a and 7b illustrate that as the quantity of CD-MNP nanocomposites increases, the intensity of the DPPH peak reduces. The observed reduction in peak intensity demonstrates the nanocomposites' capacity to effectively neutralize free radicals and mitigate oxidative stress.

In this study, the findings reveal that CD-MNP nanocomposites exhibited significant antioxidant activity, evident from their concentration-dependent capacity to scavenge DPPH free radicals. The observed antioxidant activity of these nanocomposites is likely due to the presence of CDs, which have been previously reported to possess antioxidant properties. Hu et al. demonstrated the significant antioxidant activity of graphene quantum dots for therapeutic applications(52). The integration of these nanomaterials into the nanocomposites could improve their antioxidant efficacy and render them appropriate for utilization as antioxidant agents in diverse applications. Li et al. reported that CDs derived from Maillard reaction products possessed high DPPH and hydroxyl-radical scavenging activities(53). The antioxidant properties of CDs-MNPs can be attributed to the hydrogen-donating capability of CDs. The OH functional groups present at the edge sites of CDs act as efficient hydrogen donors, enhancing the antioxidant activity of the nanocomposites. Additionally, the Sp² carbon structure aids in the delocalization and stabilization of free electrons, further boosting their antioxidant properties. The presence of surface groups, including hydroxyl, amino, and carboxyl groups, has been associated with CDs' potential to effectively neutralize DPPH and hydroxyl radicals(53, 54). Furthermore, Figure 5b illustrates the evaluation of the antioxidant activity of the nanocomposites with ascorbic acid as a standard chemical. The findings demonstrate that the nanocomposites exhibited antioxidant properties that were analogous to those of ascorbic acid, a widely recognized antioxidant agent.

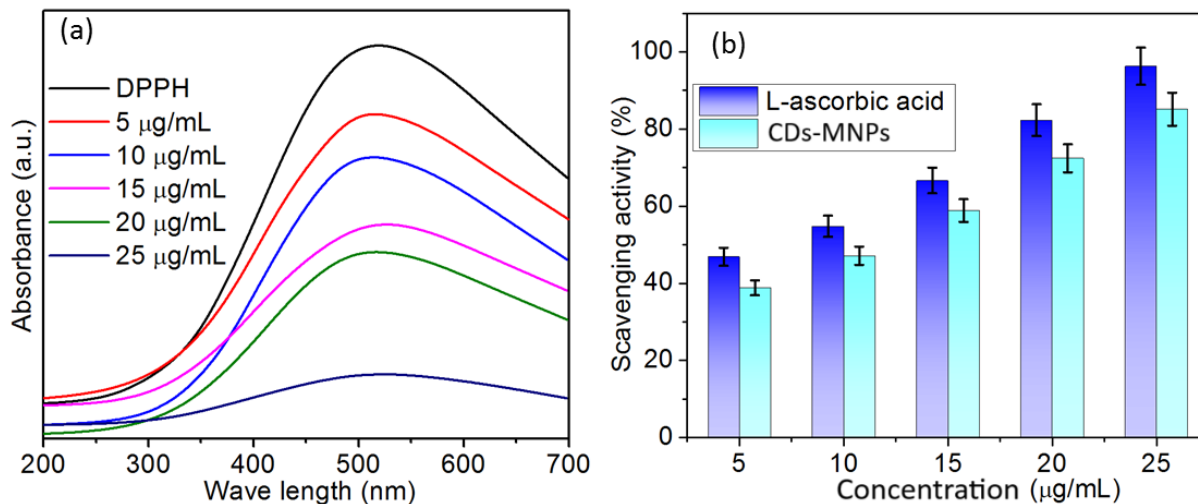


Figure 5: (a) UV–Vis spectra of DPPH radical scavenging activity of CDs-MNPs. (b) DPPH radical scavenging activity of CDs-MNPs against ascorbic acid. Data are expressed as mean \pm SD (n = 3).

Drug Delivery and Kinetics Study

The interactions among curcumin and CDs-MNPs are of utmost importance in the release mechanism, which is reliant on pH. Given its hydrophobic characteristics, curcumin demonstrates robust π - π stacking interactions and hydrophobic interactions with the carbon dots (Figure 8). These interactions facilitate the entrapment of the medication within the hydrophobic regions of the CDs. In addition, the magnetic nanoparticles enhance the stability and structural integrity of the composite, guaranteeing a consistent release profile throughout time (55, 56). The regulated release of curcumin is also influenced by the electrostatic interactions between the functional groups on the CDs and the somewhat ionizable curcumin. At acidic pH levels, the surface functional groups on the CDs and the drug are protonated, leading to a greater release of curcumin due to less electrostatic interactions and low encapsulation. Overall, the drug delivery system using CDs-MNPs shows a notable release of curcumin that is dependent on the pH level. The greatest release is found at pH 5, followed by pH 6.6 and pH 7.4. The distinct interplay between curcumin and the CDs-MNPs composite, involving π - π stacking, hydrophobic contacts, and electrostatic interactions, enables the achievement of this regulated release pattern. This feature renders the system very efficient for delivering drugs to specific locations in acidic conditions, offering a promising method for improving the effectiveness of curcumin in cancer treatment and other medical applications that rely on pH fluctuations.

CD-MNP composites have become a viable platform for the controlled release of therapeutic drugs based on pH levels in the development of improved drug delivery systems. These composite materials utilize the distinct characteristics of both CDs and MNPs to produce effective and regulated drug delivery. More precisely, the system's capacity to adjust the release of drugs according to the pH of its surroundings makes it especially well-suited for targeting acidic environments, such as those present in tumour tissues or inflamed regions. The medication utilized in this investigation is curcumin, a hydrophobic molecule renowned for its anti-inflammatory and anticancer characteristics. Curcumin, when combined with CDs-MNPs composite, demonstrates a release profile that is sensitive to changes in pH (see Figure 9a). The release of curcumin from the CDs-MNPs system is dependent on the pH level. The maximum amount of curcumin is released at pH 5, followed by pH 6.6 and pH 7.4. At a pH of less than 5, which replicates the acidic conditions found in tumour tissues, the total amount released reaches approximately 85%. This high release rate is due to the enhanced solubility and ionization of curcumin in acidic environments, which promotes its diffusion from the nanoparticles. At pH 6.6 which indicates the mildly acidic environment commonly present in inflamed or malignant tissues, the total release amounts to ~66%. At a pH of 7.4, which is the normal pH level found in healthy tissues, the release rate is reduced ~58%; this suggests that the release is better regulated and aimed towards non-specific locations.

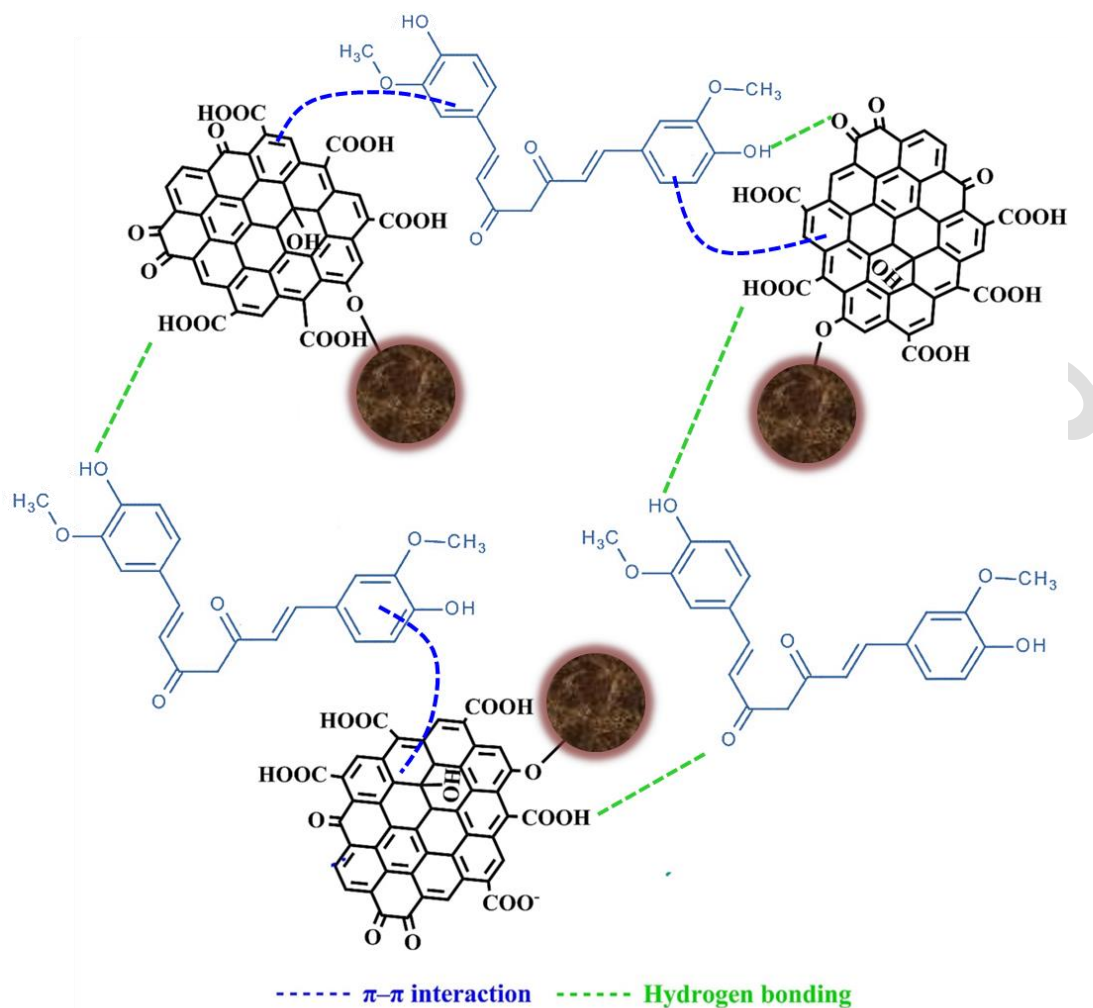


Figure 6: Proposed loading mechanism of curcumin onto CDs-MNPs nanocomposites.

The release profiles of curcumin from the composite of CDs-MNPs were analyzed at three pH levels (5, 6.6, and 7.4) using the zero-order Donbrow–Samuelov model. This analysis aimed to determine the kinetics of drug release. This model, commonly used to assess the release kinetics of controlled drug delivery systems, offers valuable information on the rate of drug release over time, assuming a consistent release rate independent of drug concentration. The mathematical expression for the zero-order Donbrow–Samuelov model is as follows:

$$M_t = M_0 + k_0 t \quad (1)$$

where M_t , M_0 , and k_0 correspond to the cumulative release (%) at time 't', initial amount of drug, and zero order rate constant, respectively.

The release data at pH 5, 6.6, and 7.4 was examined to determine how well it conformed to the zero-order Donbrow–Samuelov model. The progressive liberation of curcumin from the CDs-MNPs composite was quantified over a period of time and graphically represented for each pH level, as depicted in Figure 9b. At a pH of 5, the release profile demonstrates the maximum cumulative release, reaching over 85% of the entire medication injected during a certain time period. The data was fitted to the zero-order model, resulting in a linear plot with a high correlation coefficient in 60% of the release data ($R^2 \approx 0.98$), indicating a strong fit. The release constant was determined to be around 0.85% per hour, indicating the consistent and regulated release of curcumin in an acidic environment. The rapid release of curcumin at pH 5 can be explained by the enhanced solubility and ionization of the compound in acidic environments, which promote its diffusion from the nanoparticles.

At a pH of 6.6, the rate of release was marginally reduced, resulting in a cumulative release of approximately 65%. The data fitting revealed a release constant of roughly 0.65% per hour. This indicates that the release mechanism remains constant at different pH levels; however, there are differences in the rate of release due to changes in the ionization state of curcumin and the surface characteristics of the CDs-MNPs composite. The pH of 6.6, which is slightly acidic, imitates the conditions found in inflamed or malignant tissues. This regulated release of drugs is advantageous for delivering them specifically to the affected areas.

At a pH of 7.4, the total release was minimal, around 50%. The reduced release rate at neutral pH suggests that the CDs-MNPs composite effectively regulates the release of drugs in healthy tissue settings, minimizing the risk of early drug release and improving the precision of the drug delivery system. The fluctuations in the release constants at various pH levels demonstrate the impact of the surrounding environment on the kinetics of drug release. Higher release rates are advantageous in acidic environments with a pH of 5 and 6.6 as they can effectively target tumours or inflamed tissues; this is because the acidic milieu in these tissues can stimulate a quicker release of the drug. Conversely, the decreased rate of medication release at pH 7.4 is advantageous for limiting the release of the drug in healthy tissues, thus decreasing the likelihood of adverse effects and improving the medicine's therapeutic effectiveness. The release behaviour in different pHs is also depicted graphically in Figure 10a.

The release patterns of curcumin from the composite of CDs-MNPs were examined at various pH levels (5, 6.6, and 7.4) and then fitted to the Higuchi model. This model is frequently employed to

elucidate the liberation of pharmaceuticals from diverse matrices, offering valuable understanding of the drug diffusion mechanism and the impact of matrix structure on the kinetics of drug release. The following equation represents the Higuchi model, which was developed in 1961 (57):

$$Q_t = k_H t^{\frac{1}{2}} \quad (2)$$

where $Q(t)$ represents the cumulative amount of drug released at time t and k_H is the Higuchi dissolution constant, indicative of the drug release rate.

At a pH of 5, the release profile of curcumin is highly noticeable, with a cumulative release of almost 85% during the observed time period (Figure 9c). The elevated k_H value observed at pH 5 is in line with the enhanced solubility and diffusion of curcumin in an acidic milieu, promoting its swift liberation from the CDs-MNPs composite. At a pH of 6.6, which indicates a mildly acidic environment, around 65% of curcumin was released. This indicates that the release mechanism at pH 6.6 is predominantly governed by diffusion, albeit at a slower pace in comparison to pH 5. The decreased k_H value indicates the decreased solubility and diffusion rate of curcumin at this pH level, resulting in a more precise release that is appropriate for targeting inflammatory or malignant areas. At a pH of 7.4, the total amount of curcumin released is minimal at approximately 50%. The application of the Higuchi model to the release data yielded a correlation coefficient ($R^2 \approx 0.93$) and a Higuchi constant k_H of around 5.0% per hour. The decreased k_H value at pH 7.4 indicates a slower and more regulated release in neutral conditions, which is advantageous for reducing the early release of curcumin in normal tissues and improving the precision of the drug delivery system.

The analysis of the release data using the Korsmeyer–Peppas model indicates that the release of curcumin from the CDs-MNPs composite follows an abnormal transport mechanism at all pH levels. The operational Korsmeyer–Peppas model is as follows:

$$F(D) = k_{KP} t^n \quad (3)$$

$Q(t)$ represents the amount of medication that has been supplied at a certain time 't', while 'k' is a constant. The constant k_{KP} incorporates the shape-related characteristics of the molecular carrier, including its morphology. The release exponent, denoted as n , characterizes the release pattern. The variable n reveals how carbon dots release drugs. The magnitude of n defines whether the release is primarily governed by diffusion through the nanoparticles, exterior erosion, or a combined effect of both. The Korsmeyer–Peppas model (Figure 9d) was used to fit the cumulative release data for curcumin-loaded CDs-MNPs. The resulting K_{KP} values ranged from 0.15 to 0.25

(Figure 9e). The data indicate that the release mechanism is controlled by diffusion, and it is highly responsive to changes in the environment at pH levels 5, 6.6, and 7.4. This ensures that the drug delivery is both targeted and efficient. The range of values of the release exponent 'n' from 0.35 to 0.55 indicate that both diffusion through the matrix and relaxing of the nanoparticle structure play a role in the overall release process. The presence of this dual mechanism provides a benefit in maintaining a controlled release profile that may be adjusted in response to changes in environmental pH. In the context of the Korsmeyer–Peppas model for drug release kinetics, a release exponent value of 0.45 (Figure 9f) typically indicates a release mechanism characterized by non-Fickian or anomalous diffusion. At a pH of 5, the increased release exponent and rate constant indicate a fast release caused by the combined influence of improved diffusion and matrix relaxation in acidic circumstances. This is especially advantageous for specifically targeting acidic tumour microenvironments where a rapid release of curcumin is sought to achieve therapeutic effectiveness. At a pH of 6.6, the release mechanism is mostly controlled by anomalous transport, resulting in a moderate release rate that is appropriate for delivering curcumin to inflamed tissues. At a pH of 7.4, the release rate is slower, and there is a greater contribution from matrix relaxation mechanisms; this results in a controlled and prolonged release under neutral conditions, which reduces the likelihood of side effects and maximizes therapeutic effectiveness. Figure 9g demonstrates the schematic of drug loading and release behaviour at different pHs.

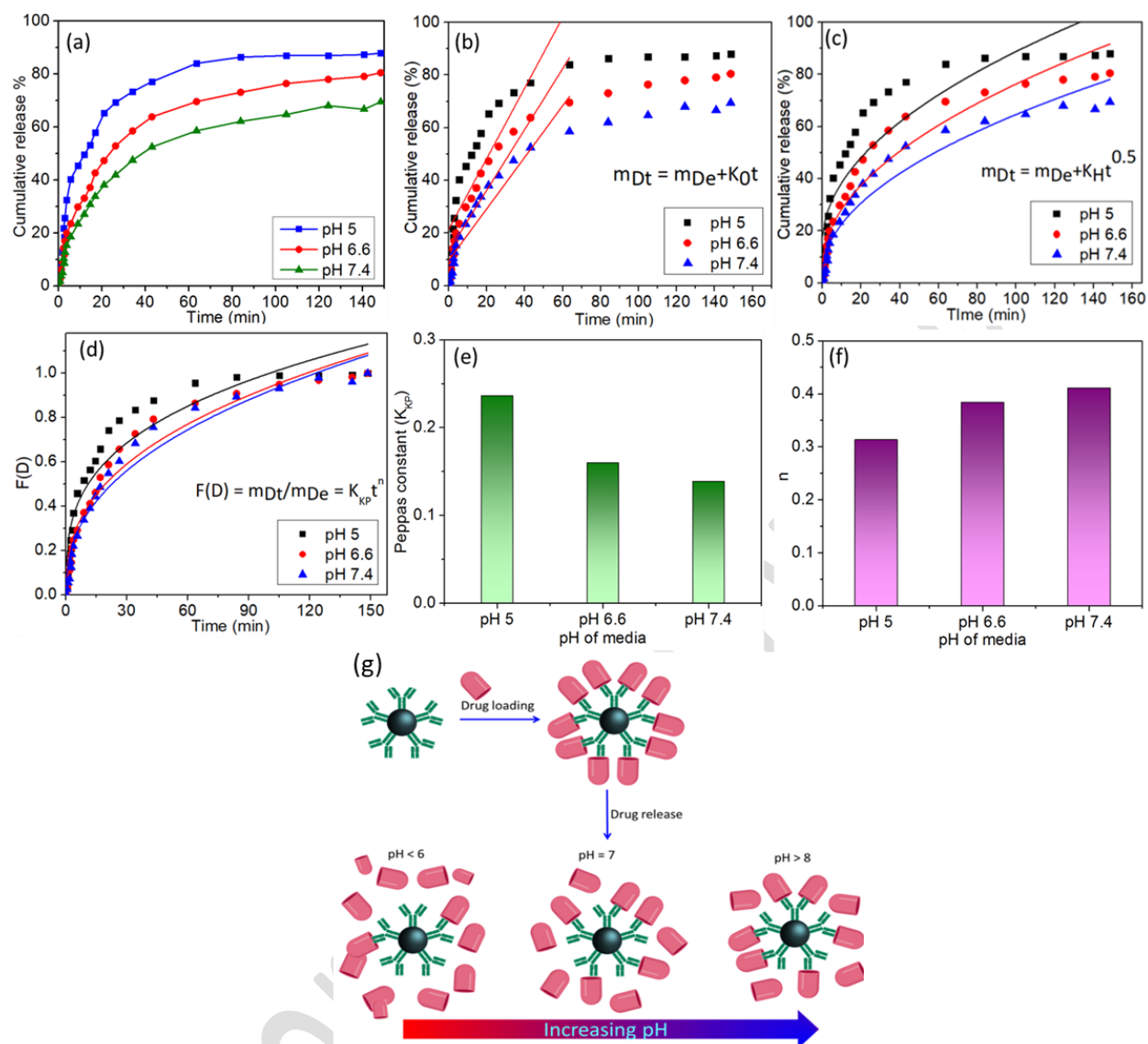


Figure 7: (a) Cumulative drug release behavior of CDs-MNPs in different pH environment. (b) Fitting of the release data in the zero-order Donbrow–Samuelov model. (c) Fitting of the release data in the Higuchi model. (d) Fitting of the release data in the Korsmeyer–Peppas model. (e) Histogram of Peppas constant at different pHs. (f) Histogram of 'n' exponent (obtained from model fittings) at different pHs. (g) Illustration of the proposed drug loading and release mechanism in CDs-MNPs. The drug is initially loaded onto the nanoparticle surface. At neutral pH (pH 7), the drug remains attached to the nanoparticles. At acidic pH (pH < 6), faster release is observed due to weaker electrostatic interactions. At basic pH (pH > 8), release is reduced, indicating stronger interactions between the drug and the nanoparticle surface. The release behavior is governed by pH-dependent interactions between curcumin and CDs-MNPs.

For instance, Kim et al. (2015) reported a rapid release of curcumin from mesoporous silica nanoparticles coated with a tannic acid–Fe(III) complex at acidic pH levels, with a more sustained release at physiological pH 7.4. This behavior was attributed to the pH-sensitive nature of the coating, which decomposes more readily in acidic environments, facilitating faster drug release (58). Similarly, a study by Aram et al. described a pH-sensitive, shell-sheddable magnetic nanocarrier where curcumin release was more pronounced at tumor-relevant acidic pH (5.6) compared to physiological pH (7.4). The authors attributed this to the shedding of the PEG corona in acidic conditions, which triggered the release of the drug (59). Furthermore, research by Sadeghi et al. (2019) demonstrated that PEGylated magnetic nanoparticles exhibited a pH-dependent curcumin release profile, with higher release observed at acidic pH (5.4) compared to neutral pH (7.4). This was attributed to the increased solubility and diffusion of curcumin in acidic environments (60). These studies support our findings that curcumin release is enhanced under acidic conditions, which is advantageous for targeting the acidic microenvironments often found in tumor tissues.

MTT Assay

The graph in Figure 10 illustrates how varying concentrations and exposure times of CDs-MNPs affect cell proliferation, as tested by the MTT assay. To evaluate cell proliferation, the degree of cell death in the presence of the sample was quantified. A cell's metabolic activity is a key factor in its healthiness. Both the concentration and period of CD-MNP exposure directly influence the rate of cell death, which consequently affects cell viability. At a concentration of 20 mg/mL, cell viability remains relatively high, with only about 2%–4% of cells being impacted. However, at a concentration of 100 mg/mL, the cell-killing percentage rises considerably. The plot reveals that the cytotoxic effect increases with time, with more cell death observed at 72 hours than at 24 hours for each concentration. These results indicate that CDs-MNPs affect cell vitality based on both the dose and the exposure duration. Longer exposure results in higher cell mortality, emphasizing the need for careful consideration of both concentration and exposure time when using CDs-MNPs.

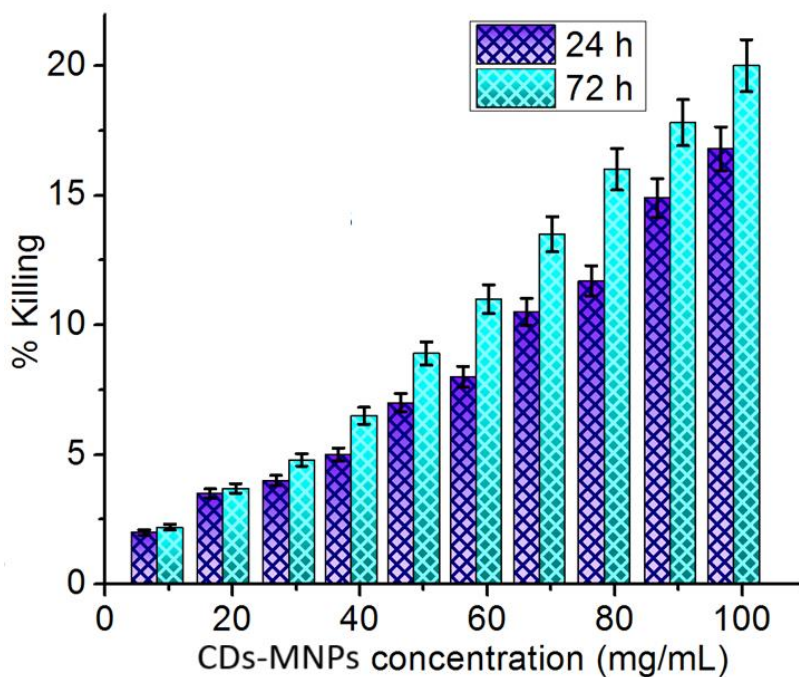


Figure 8: Cytotoxicity assay of CDs-MNPs over living cell line.

Antibacterial Activity

In this study, gram-negative bacteria *E. coli* and gram-positive bacteria *S. aureus* were used as model microorganisms to assess the antibacterial activity of CDs-MNPs. The antibacterial activity of CDs-MNPs at varying concentrations (Controls: 0 $\mu\text{g/mL}$, C1: 60 $\mu\text{g/mL}$, and C2: 170 $\mu\text{g/mL}$) was measured over time by monitoring the optical density at 600 nm (OD600), per Figure 11. A notable decline in bacterial growth rates was recorded with increasing doses of CDs-MNPs, while the control group had a higher growth rate, reaching its maximum OD600 values. The results demonstrate that higher concentrations of CDs-MNPs improve their interaction with bacterial cell walls, effectively inhibiting bacterial growth. Travlou et al. investigated the antibacterial activity of CDs against *E. coli* and *B. subtilis* and discovered that CDs' antibacterial properties are significantly influenced by their physicochemical properties and dimensions at the nanoscale(61). The study emphasized the importance of the nitrogen functional groups found on the surface of CDs in determining their antibacterial activity. The protonated amino group interacts electrostatically with the phospholipids of the bacterial cell membrane, resulting in bacterial cell

death. The minimum inhibitory concentration (MIC) is the lowest concentration of an antibacterial agent that effectively inhibits the growth of bacteria. For *E. coli* and *S. aureus*, the MIC value has been determined to be 110 $\mu\text{g/mL}$. The enhanced interaction of MCDs with bacterial cell walls at higher concentrations can be attributed to increased surface availability, electrostatic attraction, and molecular interactions. A greater number of MCDs in the medium leads to a higher probability of contact with bacterial membranes, facilitating stronger adhesion. Since bacterial cell walls are typically negatively charged positively or partially positively charged MCDs exhibit electrostatic attraction, promoting binding. Additionally, hydrophobic interactions and hydrogen bonding between MCDs and membrane components further enhance attachment (62). At elevated concentrations, MCDs may form a dense layer around bacterial cells, increasing localized interactions and potentially leading to membrane disruption or oxidative stress. Furthermore, a higher concentration of MCDs enhances adsorption onto bacterial surfaces or facilitates internalization, amplifying their effect. These combined factors contribute to the improved bacterial interaction observed in our study.

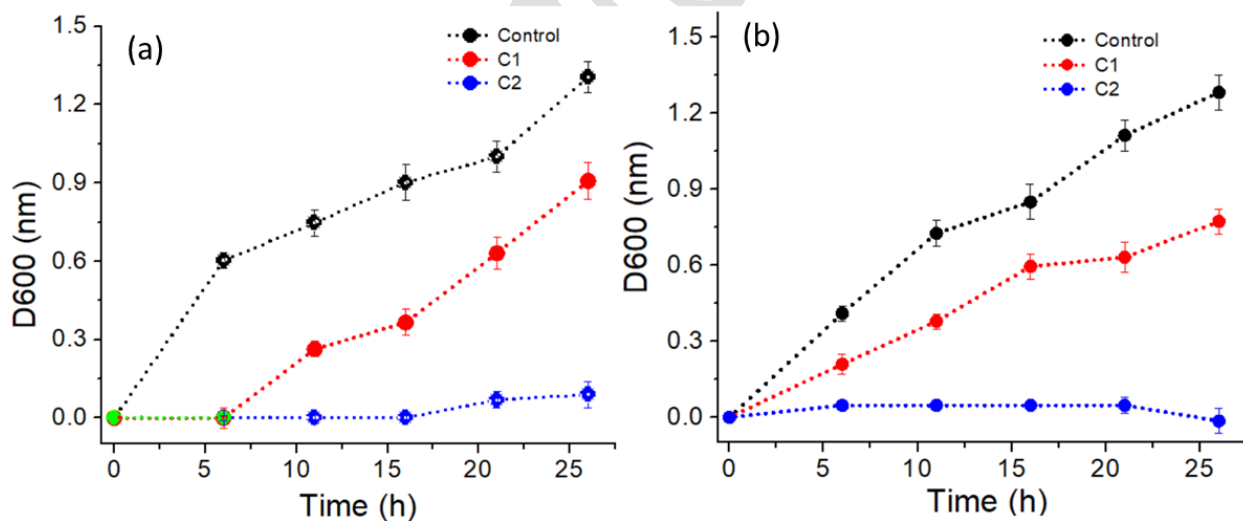


Figure 9: Growth curves of bacteria indicating the inhibitory effects of CD-MNP concentrations on the growth of (a) *E. coli* and (b) *S. aureus*, respectively. (Controls: 0 $\mu\text{g/mL}$, C1: 60 $\mu\text{g/mL}$, and C2: 170 $\mu\text{g/mL}$)

Conclusions

The present study effectively produced and thoroughly characterized magnetic N-doped carbon dots utilizing a range of techniques, including SEM, SQUID, FTIR, XRD, CW-EPR, XPS, BET, and TGA. The characterizations provide confirmation of the structural, magnetic, chemical, and thermal properties of the produced CDs-MNPs, which are essential for their use in biological applications. The synthesized CDs-MNPs demonstrated a pH-responsive nature (pH 5–7.4), rendering them ideal contenders for targeted drug delivery systems. The drug release investigations, utilizing the zero-order, Higuchi, and Peppas models, exhibited sustained and controlled release patterns. This emphasizes the potential of CDs-MNPs as effective carriers for drugs. The antioxidant experiments demonstrated that CDs-MNPs possess notable scavenging capacity (more than 80%), suggesting their potential use in treating disorders associated with oxidative stress. The observed antioxidant behaviour was ascribed to the existence of nitrogen doping and carbon dot functionalities, which augmented their ability to scavenge radicals. Moreover, the biocompatibility of CDs-MNPs was confirmed through cytotoxicity studies using MTT assays at the concentrations studied. This confirms that CDs-MNPs are safe for prospective biomedical applications. The MTT assay results were also shown to be consistent with the drug release profiles, highlighting the significance of controlled release in preserving cell viability. Overall, the synthesized CDs-MNPs present potential as drug delivery vehicles that respond to changes in pH and have natural antioxidant characteristics. This makes them a versatile platform for targeted therapy and managing oxidative stress in biomedical applications. The CDs-MNPs yielded a significant reduction in bacterial growth rates with increasing dosages for both *E. coli* and *S. aureus*. Future research could focus on in vivo assessments to further explore the effectiveness of these materials for potential therapeutic applications.

Availability of data and materials: The datasets used and analyzed during the current study are available from the corresponding author on reasonable request.

Funding: This research is funded by King Saud University, Riyadh, Saudi Arabia.

Supplementary data: In the supplementary file, Antioxidant Activity measurement, Antibacterial Activity Evaluation, UV-vis absorption spectra, TEM images of nanoparticles, Digital images of DPPH and after DPPH activity are given.

Authors' contributions: Conceptualization, Hayat Alzahrani, Tawfiq Alsulami, Abdulhakeem Alzahrani and Suleiman Althawab; Formal analysis, Hayat Alzahrani, Tawfiq Alsulami and Suleiman Althawab; Investigation, Hayat Alzahrani, Tawfiq Alsulami and Suleiman Althawab; Methodology, Tawfiq Alsulami, Abdulhakeem Alzahrani and Suleiman Althawab; Resources, Mohammed Alkaltham; Software, Tawfiq Alsulami; Supervision, Suleiman Althawab; Validation, Hayat Alzahrani and Tawfiq Alsulami; Visualization, Hayat Alzahrani, Mohammed Alkaltham and Abdulhakeem Alzahrani; Writing – original draft, Hayat Alzahrani, Mohammed Alkaltham and Suleiman Althawab; Writing – review & editing, Abdulhakeem Alzahrani.

Declaration of competing interest

The authors declare that they have no known competing financial interests or personal relationships that could have appeared to influence the work reported in this paper.

Acknowledgements: The authors would like to extend their sincere appreciation to the Researchers Supporting Project, King Saud University, Riyadh, Saudi Arabia, for funding this work through the project number (RSPD2025R589).

References

1. B. Wang, and S. Lu, The light of carbon dots: from mechanism to applications, *Matter* **5** (2022) 110–149; <https://doi.org/10.1016/j.matt.2021.10.016>
2. S. Ganguly, P. Das, S. Banerjee, and N.C. Das, Advancement in science and technology of carbon dot-polymer hybrid composites: a review, *Funct. Compos. Struct.* **1** (2019) 022001; <https://doi.org/10.1088/2631-6331/ab0c80>
3. M. Kurian, and A. Paul, Recent trends in the use of green sources for carbon dot synthesis – a short review, *Carbon Trends* **3** (2021) 100032; <https://doi.org/10.1016/j.cartre.2021.100032>
4. G. Ge, L. Li, D. Wang, M. Chen, Z. Zeng, W. Xiong, X. Wu, and C. Guo, Carbon dots: synthesis, properties and biomedical applications, *J. Mater. Chem. B* **9** (2021) 6553–6575; <https://doi.org/10.1039/D1TB01077H>
5. P. Das, S. Ganguly, S. Banerjee, and N.C. Das, Graphene based emergent nanolights: a short review on the synthesis, properties and application, *Res. Chem. Intermed.* **45** (2019) 3823–3853; <https://doi.org/10.1007/s11164-019-03823-2>

6. P. Das, S.R. Ahmed, S. Srinivasan, and A.R. Rajabzadeh, Optical properties of quantum dots, in: *Quantum Dots and Polymer Nanocomposites*, CRC Press, 2022, pp. 69–85.
7. M. Zulfajri, S. Sudewi, S. Ismulyati, A. Rasool, M. Adlim, and G.G. Huang, Carbon dot/polymer composites with various precursors and their sensing applications: a review, *Coatings* **11** (2021) 1100; <https://doi.org/10.3390/coatings11091100>
8. J. Wang, and J. Qiu, A review of carbon dots in biological applications, *J. Mater. Sci.* **51** (2016) 4728–4738; <https://doi.org/10.1007/s10853-016-9797-7>
9. T. Lv, L. Pan, X. Liu, T. Lu, G. Zhu, Z. Sun, and C.Q. Sun, One-step synthesis of CdS–TiO₂–chemically reduced graphene oxide composites via microwave-assisted reaction for visible-light photocatalytic degradation of methyl orange, *Catal. Sci. Technol.* **2** (2012) 754–758; <https://doi.org/10.1039/C2CY00452F>
10. V. Ahuja, A.K. Bhatt, S. Varjani, K.-Y. Choi, S.-H. Kim, Y.-H. Yang, and S.K. Bhatia, Quantum dot synthesis from waste biomass and its applications in energy and bioremediation, *Chemosphere* **293** (2022) 133564; <https://doi.org/10.1016/j.chemosphere.2022.133564>
11. S.A. Shaik, S. Sengupta, R.S. Varma, M.B. Gawande, and A. Goswami, Syntheses of N-doped carbon quantum dots (NCQDs) from bioderived precursors: a timely update, *ACS Sustain. Chem. Eng.* **9** (2020) 3–49; <https://doi.org/10.1021/acssuschemeng.0c04727>
12. L. Behera, D. Pati, B.B. Sahu, and S. Mohapatra, One-step synthesis of Mn-carbon dot nanoprobe for signal-on detection of arsenic and reversible temperature sensing, *Colloids Surf. A* **653** (2022) 130002; <https://doi.org/10.1016/j.colsurfa.2022.130002>
13. A.A. Madhavan, D. Kushwaha, D. Nath, R. Ghosh Moulick, and J. Bhattacharya, Natural occurrence of carbon dots during in vitro nonenzymatic glycosylation of hemoglobin A₀, *ACS Omega* **7** (2022) 3881–3888; <https://doi.org/10.1021/acsomega.1c03219>
14. H. Li, X. Yan, D. Kong, R. Jin, C. Sun, D. Du, Y. Lin, and G. Lu, Recent advances in carbon dots for bioimaging applications, *Nanoscale Horiz.* **5** (2020) 218–234; <https://doi.org/10.1039/C9NH00476A>
15. G.A. Hutton, B.C. Martindale, and E. Reisner, Carbon dots as photosensitisers for solar-driven catalysis, *Chem. Soc. Rev.* **46** (2017) 6111–6123; <https://doi.org/10.1039/C7CS00235A>
16. V. Sharma, P. Tiwari, and S.M. Mobin, Sustainable carbon-dots: recent advances in green carbon dots for sensing and bioimaging, *J. Mater. Chem. B* **5** (2017) 8904–8924; <https://doi.org/10.1039/C7TB02484C>
17. S. Ganguly, P. Das, S. Das, U. Ghorai, M. Bose, S. Ghosh, M. Mondal, A.K. Das, S. Banerjee, and N.C. Das, Microwave assisted green synthesis of zwitterionic photoluminescent N-doped carbon dots: an efficient ‘on-off’ chemosensor for tracer Cr(+6) considering the inner filter effect and nano drug-delivery vector, *Colloids Surf. A* **579** (2019) 123604; <https://doi.org/10.1016/j.colsurfa.2019.123604>
18. S. Ganguly, P. Das, E. Itzhaki, E. Hadad, A. Gedanken, and S. Margel, Microwave-synthesized polysaccharide-derived carbon dots as therapeutic cargoes and toughening agents for elastomeric gels, *ACS Appl. Mater. Interfaces* **12** (2020) 51940–51951; <https://doi.org/10.1021/acsaami.0c14527>
19. S.K. Debnath, and R. Srivastava, Drug delivery with carbon-based nanomaterials as versatile nanocarriers: progress and prospects, *Front. Nanotechnol.* **3** (2021) 644564; <https://doi.org/10.3389/fnano.2021.644564>

20. Q. Wang, X. Huang, Y. Long, X. Wang, H. Zhang, R. Zhu, L. Liang, P. Teng, and H. Zheng, Hollow luminescent carbon dots for drug delivery, *Carbon* **59** (2013) 192–199; <https://doi.org/10.1016/j.carbon.2013.03.009>
21. X. Jia, M. Pei, X. Zhao, K. Tian, T. Zhou, and P. Liu, PEGylated oxidized alginate-DOX prodrug conjugate nanoparticles cross-linked with fluorescent carbon dots for tumor theranostics, *ACS Biomater. Sci. Eng.* **2** (2016) 1641–1648; <https://doi.org/10.1021/acsbiomaterials.6b00443>
22. D. Guimarães, A. Cavaco-Paulo, and E. Nogueira, Design of liposomes as drug delivery system for therapeutic applications, *Int. J. Pharm.* **601** (2021) 120571; <https://doi.org/10.1016/j.ijpharm.2021.120571>
23. S. Yasamineh, P. Yasamineh, H.G. Kalajahi, O. Gholizadeh, Z. Yekanipour, H. Afkhami, M. Eslami, A.H. Kheirkhah, M. Taghizadeh, and Y. Yazdani, A state-of-the-art review on the recent advances of niosomes as a targeted drug delivery system, *Int. J. Pharm.* **624** (2022) 121878; <https://doi.org/10.1016/j.ijpharm.2022.121878>
24. G. Shim, S. Jeong, J.L. Oh, and Y. Kang, Lipid-based nanoparticles for photosensitive drug delivery systems, *J. Pharm. Investig.* **52** (2022) 151–160; <https://doi.org/10.1007/s40005-021-00553-9>
25. M. Zu, Y. Ma, B. Cannup, D. Xie, Y. Jung, J. Zhang, C. Yang, F. Gao, D. Merlin, and B. Xiao, Oral delivery of natural active small molecules by polymeric nanoparticles for the treatment of inflammatory bowel diseases, *Adv. Drug Deliv. Rev.* **176** (2021) 113887; <https://doi.org/10.1016/j.addr.2021.113887>
26. S. Karimi and H. Namazi, A photoluminescent folic acid-derived carbon dot functionalized magnetic dendrimer as a pH-responsive carrier for targeted doxorubicin delivery, *New J. Chem.* **45**(14) (2021) 6397–6405; <https://doi.org/10.1039/D0NJ06261H>
27. B. Rani, M. Ahmad, K. Alam, F. Seidi, S. Shakeel, J. Song, Y. Jin, and H. Xiao, Recent advances in magnetic nanoparticles: Key applications, environmental insights, and future strategies, *Sustain. Mater. Technol.* **40** (2024) e00985; <https://doi.org/10.1016/j.susmat.2024.e00985>
28. C. Miriam, S.C. Romero, M.F. Casula, L. Gutiérrez, M.P. Morales, I.B. Böhm, J.T. Heverhagen, D. Prospero, and W.J. Parak, Biological applications of magnetic nanoparticles, *Chem. Soc. Rev.* **41** (2012) 4306–4334; <https://doi.org/10.1039/C2CS15337H>
29. C.V. Fernandes, A. Francesko, C. Ribeiro, M.B. López, P. Martins, and S.L. Mendez, Advances in magnetic nanoparticles for biomedical applications, *Adv. Healthc. Mater.* **7** (2018) 1700845; <https://doi.org/10.1002/adhm.201700845>
30. S.K. Kailasa and J.R. Koduru, Perspectives of magnetic nature carbon dots in analytical chemistry: From separation to detection and bioimaging, *TrAC Trends Environ. Anal. Chem.* **33** (2022) e00153; <https://doi.org/10.1016/j.teac.2021.e00153>
31. J.T. John, E.F. Nwude, S. Singh, B.G. Prajapati, D.U. Kapoor, and N. Muangsin, Sustainable synthesis of gold nanoparticles for drug delivery and cosmeceutical applications: a review, *BioNanoScience* **14** (2024) 3355–3384; <https://doi.org/10.1007/s12668-024-01436-7>
32. Y. Mehdi and H. Sabaghian, Silver nanoparticle-based drug delivery systems in the fight against COVID-19: Enhancing efficacy, reducing toxicity and improving drug bioavailability, *J. Drug Target.* **32** (2024) 794–806; <https://doi.org/10.1080/1061186X.2024.2356147>

33. N.S. Thakur, N. Saleh, A.F. Khan, B. Chakrabarty, and V. Agrahari, Progress and promise of photoresponsive nanocarriers for precision drug delivery in cancer, *J. Photochem. Photobiol. C: Photochem. Rev.* **59** (2024) 100665; <https://doi.org/10.1016/j.jphotochemrev.2024.100665>
34. Z. Zhu, R. Cheng, L. Ling, Q. Li, and S. Chen, Rapid and large-scale production of multi-fluorescence carbon dots by a magnetic hyperthermia method, *Angew. Chem. Int. Ed.* **59** (2020) 3099–3105; <https://doi.org/10.1002/anie.201914331>
35. S. Li, Q. Zhou, Z. Li, M. Liu, Y. Li, and C. Chen, Sensitive fluorescent probe based on combination of magnetic molecularly imprinted materials and carbon dots derived from Prussian blue for p-aminoazobenzene in environmental samples, *J. Clean. Prod.* **402** (2023) 136827; <https://doi.org/10.1016/j.jclepro.2023.136827>
36. X. Li, Y. Fu, S. Zhao, J. Xiao, M. Lan, B. Wang, K. Zhang, X. Song, and L. Zeng, Metal ions-doped carbon dots: Synthesis, properties, and applications, *Chem. Eng. J.* **430** (2022) 133101; <https://doi.org/10.1016/j.cej.2021.133101>
37. Y. Zhong, L. Chen, S. Yu, Y. Yang, and X. Liu, Advances in magnetic carbon dots: A theranostics platform for fluorescence/magnetic resonance bimodal imaging and therapy for tumors, *ACS Biomater. Sci. Eng.* **9** (2023) 6548–6566; <https://doi.org/10.1021/acsbiomaterials.3c00988>
38. T. Rezaei, M. Rezaei, S. Karimifard, F.M. Beram, M.S. Dakkali, M. Heydari, S.A. Behbahanizadeh et al., Folic acid-decorated pH-responsive nanoniosomes with enhanced endocytosis for breast cancer therapy: in vitro studies, *Front. Pharmacol.* **13** (2022) 851242; <https://doi.org/10.3389/fphar.2022.851242>
39. N. Choi, C. Tang, Y. Park, A. Du, G.A. Ayoko, Y. Hwang, and S. Chae, Visible-light-driven photocatalytic degradation of tetracycline using citric acid and lemon juice-derived carbon quantum dots incorporated TiO₂ nanocomposites, *Sep. Purif. Technol.* **350** (2024) 127836; <https://doi.org/10.1016/j.seppur.2024.127836>
40. M.O. Besenhard, A.P. LaGrow, A. Hodzic, M. Kriechbaum, L. Panariello, G. Bais, K. Loizou, S. Damilos, M.M. Cruz, N.T.K. Thanh, and A. Gavriilidis, Co-precipitation synthesis of stable iron oxide nanoparticles with NaOH: New insights and continuous production via flow chemistry, *Chem. Eng. J.* **399** (2020) 125740; <https://doi.org/10.1016/j.cej.2020.125740>
41. S. Ganguly, Neelam, I. Grinberg, and S. Margel, Layer-by-layer controlled synthesis at room temperature of tri-modal (MRI, fluorescence and CT) core/shell superparamagnetic IO/human serum albumin nanoparticles for diagnostic applications, *Polym. Adv. Technol.* **32** (2021) 3909–3921; <https://doi.org/10.1002/pat.5344>
42. D. Amara and S. Margel, Synthesis and characterization of superparamagnetic core–shell micrometre-sized particles of narrow size distribution by a swelling process, *J. Mater. Chem.* **22** (2012) 9268–9276; <https://doi.org/10.1039/C2JM00021K>
43. R. Mohammad-Rezaei, H. Razmi, V. Abdollahi, and A.A. Matin, Preparation and characterization of Fe₃O₄/graphene quantum dots nanocomposite as an efficient adsorbent in magnetic solid phase extraction: application to determination of bisphenol A in water samples, *Anal. Methods* **6** (2014) 8413–8419; <https://doi.org/10.1039/C4AY01633E>
44. S. Ganguly and S. Margel, Design of magnetic hydrogels for hyperthermia and drug delivery, *Polymers* **13** (2021) 4259; <https://doi.org/10.3390/polym13234259>

45. Y. Köseoğlu, F. Yıldız, D.K. Kim, M. Muhammed, and B. Aktaş, EPR studies on Nano-oleate coated Fe₃O₄ nanoparticles, *Phys. Status Solidi C* **1** (2004) 3511–3515; <https://doi.org/10.1002/pssc.200405493>
46. S. Zhuo, Y. Guan, H. Li, J. Fang, P. Zhang, J. Du, and C. Zhu, Facile fabrication of fluorescent Fe-doped carbon quantum dots for dopamine sensing and bioimaging application, *Analyst* **144** (2019) 656–662; <https://doi.org/10.1039/C8AN01741G>
47. Y. Guo, D. Tang, L. Zhang, B. Li, A. Iqbal, W. Liu, and W. Qin, Synthesis of ultrathin carbon dots-coated iron oxide nanocubes decorated with silver nanoparticles and their excellent catalytic properties, *Ceram. Int.* **43** (2017) 7311–7320; <https://doi.org/10.1016/j.ceramint.2017.03.033>
48. B. Li, X. Wang, Y. Guo, A. Iqbal, Y. Dong, W. Li, W. Liu, W. Qin, S. Chen, and X. Zhou, One-pot synthesis of polyamines improved magnetism and fluorescence Fe₃O₄-carbon dots hybrid NPs for dual modal imaging, *Dalton Trans.* **45** (2016) 5484–5491; <https://doi.org/10.1039/C5DT04488J>
49. C. Han, A. Zhang, Y. Kong, N. Yu, T. Xie, B. Dou, K. Li, Y. Wang, J. Li, and K. Xu, Multifunctional iron oxide-carbon hybrid nanoparticles for targeted fluorescent/MR dual-modal imaging and detection of breast cancer cells, *Anal. Chim. Acta* **1067** (2019) 115–128; <https://doi.org/10.1016/j.aca.2019.03.054>
50. E.R. Monazam, R.W. Breault, and R. Siriwardane, Kinetics of magnetite (Fe₃O₄) oxidation to hematite (Fe₂O₃) in air for chemical looping combustion, *Ind. Eng. Chem. Res.* **53** (2014) 13320–13328; <https://doi.org/10.1021/ie501536s>
51. G. Gnanaprakash, S. Ayyappan, T. Jayakumar, J. Philip, and B. Raj, Magnetic nanoparticles with enhanced γ -Fe₂O₃ to α -Fe₂O₃ phase transition temperature, *Nanotechnology* **17** (2006) 5851; <https://doi.org/10.1088/0957-4484/17/23/023>
52. X. Hu, X.-Y. Ma, J. Tian, and Z. Huang, Rapid and facile synthesis of graphene quantum dots with high antioxidant activity, *Inorg. Chem. Commun.* **122** (2020) 108288; <https://doi.org/10.1016/j.inoche.2020.108288>
53. D. Li, X. Na, H. Wang, Y. Xie, S. Cong, Y. Song, X. Xu, B.-W. Zhu, and M. Tan, Fluorescent carbon dots derived from Maillard reaction products: their properties, biodistribution, cytotoxicity, and antioxidant activity, *J. Agric. Food Chem.* **66** (2018) 1569–1575; <https://doi.org/10.1021/acs.jafc.7b05643>
54. P. Das, S. Ganguly, S. Margel, and A. Gedanken, Tailor-made magnetic nanolights: Fabrication to cancer theranostics applications, *Nanoscale Adv.* **3** (2021) 6762–6796; <https://doi.org/10.1039/D1NA00447F>
55. Y. Zou, Z. Sun, Q. Wang, Y. Ju, N. Sun, Q. Yue, Y. Deng, S. Liu, S. Yang, Z. Wang, F. Li, Y. Hou, C. Deng, D. Ling, and Y. Deng, Core-shell magnetic particles: Tailored synthesis and applications, *Chem. Rev.* **125** (2024) 972–1048; <https://doi.org/10.1021/acs.chemrev.4c00710>
56. R.Y. Mushtaq, N.R. Naveen, K.J. Rolla, H.A. Shmrany, S. Alshehri, A. Salawi, M. Kurakula, M.A. Alghamdi, W.Y. Rizg, R.B. Bakhaidar, W.A. Abualsunun, K.M. Hosny, and A.J. Alamoudi, Design and evaluation of magnetic-targeted bilosomal gel for rheumatoid arthritis: flurbiprofen delivery using superparamagnetic iron oxide nanoparticles, *Front. Pharmacol.* **15** (2024) 1433734; <https://doi.org/10.3389/fphar.2024.1433734>

57. M.R. Brophy and P. Deasy, Application of the Higuchi model for drug release from dispersed matrices to particles of general shape, *Int. J. Pharm.* **37** (1987) 41–47; [https://doi.org/10.1016/0378-5173\(87\)90008-1](https://doi.org/10.1016/0378-5173(87)90008-1)
58. S. Kim, S. Philippet, S. Fontanay, R.E. Duval, E. Lamouroux, N. Canilho and A. Pasc, pH- and glutathione-responsive release of curcumin from mesoporous silica nanoparticles coated using tannic acid–Fe(III) complex, *RSC Adv.* **5** (2015) 90550–90558; <https://doi.org/10.1039/C5RA16004A>
59. E. Aram, H.S. Abandansari, F. Radmanesh, H.R. Khorasani, M.R. Nowroozi, A. Hassanpour, H. Baharvand and D. Sabour, Shell-sheddable and charge-switchable magnetic nanoparticle as pH-sensitive nanocarrier for targeted drug delivery applications, *Polym. Adv. Technol.* **35** (2024) e6366; <https://doi.org/10.1002/pat.6366>
60. M. Ayubi, M. Karimi, S. Abdpour, K. Rostamizadeh, M. Parsa, M. Zamani and A. Saedi, Magnetic nanoparticles decorated with PEGylated curcumin as dual-targeted drug delivery: Synthesis, toxicity and biocompatibility study, *Mater. Sci. Eng. C* **104** (2019) 109810; <https://doi.org/10.1016/j.msec.2019.109810>
61. N.A. Travlou, D.A. Giannakoudakis, M. Algarra, A.M. Labella, E. Rodríguez-Castellón and T.J. Badosz, S- and N-doped carbon quantum dots: Surface chemistry dependent antibacterial activity, *Carbon* **135** (2018) 104–111; <https://doi.org/10.1016/j.carbon.2018.04.018>
62. B.C. Chung, E.H. Mashalidis, T. Tanino, M. Kim, A. Matsuda, J. Hong, S. Ichikawa and S.Y. Lee, Structural insights into inhibition of lipid I production in bacterial cell wall synthesis, *Nature* **533** (2016) 557–560; <https://doi.org/10.1038/nature17636>